International Journal of Non-Linear Mechanics 118 (2020) 103273

Contents lists available at ScienceDirect

International Journal of Non-Linear Mechanics

journal homepage: www.elsevier.com/locate/nlm

Multi-stable nonlinear energy sink for rotor system

Hongliang Yao *, Yuwei Wang, Yanbo Cao, Bangchun Wen

School of Mechanical Engineering and Automation, Northeastern University, Shenyang, 110819, PR China

ARTICLE INFO

Keywords:
Nonlinear energy sink
Rotor system
Piecewise linear stiffness
multi-stable

ABSTRACT

A multi-stable nonlinear energy sink (MNES) with piecewise linear stiffness and magnet negative stiffness is developed to suppress the vibration of unbalanced rotor system. The specific structure of the MNES is developed, and the working principles of the piecewise linear stiffness and negative stiffness are introduced. Then, the dynamic equations of the rotor-MNES system are established. Based on these, the transient and steady state responses of the rotor-MNES system are numerically studied. In addition, the vibration suppression ability of the MNES is analysed and compared with that of bi-stable nonlinear energy sink (BNES). Finally, experiments are carried out to verify the effectiveness of the MNES. The numerical and experimental results show that the designed MNES has a strong vibration suppress ability and can withstand a wide range of energy.

1. Introduction

Vibration absorption is an important way of vibration suppression for rotor system. By adding an absorber, which is usually a small mass, the vibration of rotor system can be 'absorbed' by resonance of the absorber. Rotor absorbers can be divided into passive type [1] and semi-active (or active) type [2]. Although the passive and semi-active (or active) type rotor absorbers are efficient in vibration suppression, both types have shortcomings: passive absorbers can only work within a narrow frequency band near the anti-resonance point, while the semi-active (or active) absorber are all complicated in structure.

Nonlinear energy sink (NES) [3–5], unlike traditional absorbers, can suppress vibration in a wide frequency range and has the potential to be the next generation of passive vibration suppression approach for rotor systems. At present, NESs can be divided into two types: ungrounded NESs and grounded NESs. The ungrounded NESs are nonlinearly coupled with the main system through the small mass, while the grounded NESs are linearly coupled to the main system and nonlinear coupled to the ground. With NES, vibration energy of the main system is transmitted to the small mass by targeted energy transfer (TET) mechanism [6–8], in which courses the transmitted energy is directly consumed by the NES damping and no longer returns to the main system. The NES has the characteristics of small mass, high reliability and wide suppression frequency band. Therefore, various types of NESs have been applied in aerospace [9], rotating machinery [10], architecture [11] and other fields.

In terms of rotor systems or rotating machines, the study of vibration suppression by NES has been studied for a long time. For example, Gourc et al. examined the effect of a NES on reducing chatter vibration in turning processes [12]. Bab et al., meanwhile, studied the vibration suppression ability of NES for a rotating beam [13]. Bergeot et al. analysed the steady-state response of helicopter blades with NES [14,15]. Yao et al. designed a new NES with permanent magnetic springs and coil springs for unbalanced rotor system [16]. The above researches have fully illustrated the effectiveness of the NES for vibration suppression of rotor system. However, although better than absorber, the traditional NES still has a narrow energy threshold corresponding to a strong nonlinear response, thereby limiting its wide range of engineering applications.

In order to further expand the engineering applications and solve the limitation of the narrow threshold, bi-stable nonlinear energy sink (BNES) [17,18] is developed. Under usual conditions, the BNES is composed of negative stiffness [19] and linear stiffness and have two equilibrium points. Many BNESs have been applied to vibration suppression [17,20] and energy harvest processes [21]. For example, Romeo et al. used numerical simulations to prove that the BNES has great damping effect on the transient response of the main system with different initial energies [17]; Habib et al. developed an adjustable BNES and applied it to suppress vibration of a two-degree-of-freedom main system [20]; Wang et al. designed a two-degree-of-freedom bi-stable piezoelectric energy harvester to verify that it can absorb the two-order resonance energy of the main system [21].

The BNES breaks through the narrow limitation of the energy threshold, and multi-stable nonlinear energy sinks (MNES) [22] expands the threshold limitation further. Compared with the BNES, the MNES has more equilibrium positions and stronger energy absorption capacity [22]. Many applications of the MNES are focused on energy harvesters, such as Tri-stable energy harvesters [23–25], Quad-stable energy harvesters [26,27].

* Corresponding author.
E-mail address: hlyao@mail.neu.edu.cn (H. Yao).

https://doi.org/10.1016/j.ijnonlinmec.2019.103273
Received 27 January 2019; Received in revised form 6 September 2019; Accepted 6 September 2019
Available online 12 September 2019

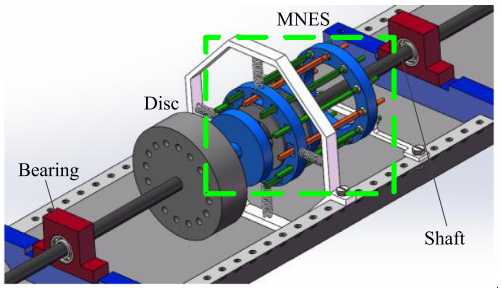

(a) The whole physical structure of the rotor-MNES system

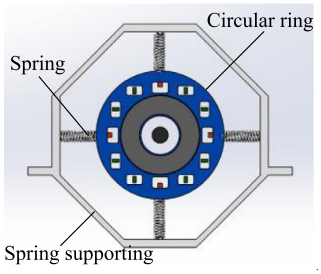

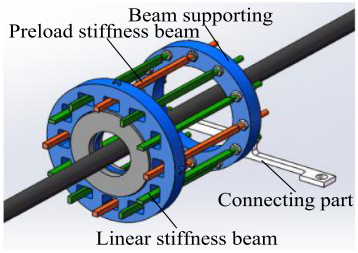

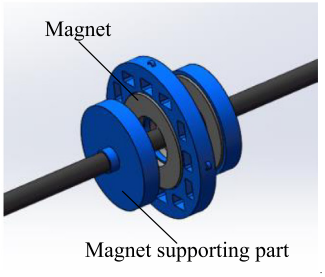

(b) MNES mass part structure (c) Piecewise stiffness part structure (d) Negative stiffness part structure

Fig. 1. Whole physical structure of the rotor-MNES system and its component structures.

At present, there is no MNES applied to the rotor vibration suppression. Therefore, in this paper a MNES for rotor system is proposed, and its structural characteristics, stiffness variation, vibration characteristics and vibration suppression effects are studied.

2. Structure and dynamic model of the rotor-MNES

2.1. Structure of the rotor-MNES system

As shown in Fig. 1(a), the MNES is mounted on the single-span-single-disc rotor system. The MNES is made up of three parts: MNES mass part, piecewise stiffness part and negative stiffness part. During working, the MNES is fixed on the test rig and does not contact with the rotor shaft, so the MNES will not rotate with the rotor.

The MNES mass part contains a circular ring and a mass supporting, as shown in Fig. 1(b). The circular ring has 12 rectangular through-holes uniformly distributed. The mass supporting consists of a supporting and four weakly stiffness springs. The springs are designed to prevent the MNES mass from rotating.

As shown in Fig. 1(c), the piecewise stiffness part contains four preload beams and eight linear beams. The preload beams are square section and the linear beams are rectangular section. One end of the preload beams and linear beams is fixed to the beam supporting. The other end of preload beams is compressed into rectangular through holes and has a certain preload. At the same time, the other end of linear beams is placed at the centre of the MNES mass rectangular through holes.

The negative stiffness part contains two magnet supporting parts and four magnets, as shown in Fig. 1(d). The magnets are fixed on the inner sides of the magnet supporting parts and on both sides of the circular ring.

2.2. Multi-stable stiffness of the MNES

The multi-stable piecewise linear force of the MNES is composed of two parts: positive force and negative force. The relationship between the multi-stable piecewise linear force of the MNES and its displacement can be expressed as

$$F_d(e) = F_z(e) + F_f(e) \tag{1}$$

where, F_d is the multi-stable piecewise linear force of the MNES. F_z is the piecewise linear positive force and F_f is the magnetic spring negative force. e is the MNES displacement in the horizontal or vertical direction.

The piecewise linear positive force F_z is provided by the combination of four preload beams, eight linear beams and four soft springs. The stiffness of soft spring k_c is very small, so its stiffness is neglected.

As shown in Fig. 2, F_r, F_x and F_y represent the forces generated by the rotor system, the horizontal stiffness beams and the vertical stiffness beams, respectively. Without considering friction, the horizontal stiffness beams and vertical stiffness beams do not interfere with each other, and they all only provide a unidirectional force. The force generated by the rotor system is decomposed into vertical and horizontal directions, so the MNES's horizontal and vertical beams can balance them in the horizontal and vertical directions, respectively.

In terms of the vertical or horizontal vibration of the rotor system, when the vibration is small (Fig. 2(a)), two preload beams provide the positive stiffness of the MNES. When the vibration is middle (Fig. 2(b)), the preload of a preload beam is completely released, and it is separated from the contact of the MNES. At this time, only one preload beam provides the positive stiffness. When the vibration is large (Fig. 2(c)), the linear beams are in contact with the MNES. Under this condition, four linear beams and a preload beam provide the positive stiffness together.

So, the positive stiffness in horizontal and vertical directions can be expressed as

$$k_z(e) = \begin{cases} 2k_a & (|e| \le e_a) \\ k_a & (e_a \le |e| \le e_b) \\ k_a + 4k_b & (|e| > e_b) \end{cases} \tag{2}$$

where, k_z, k_a and k_b represent the positive stiffness, the stiffness of preload beams and the stiffness of linear beams, respectively. e_a and e_b represent the preload compression value and the clearance distance between the linear beam and the MNES mass, respectively.

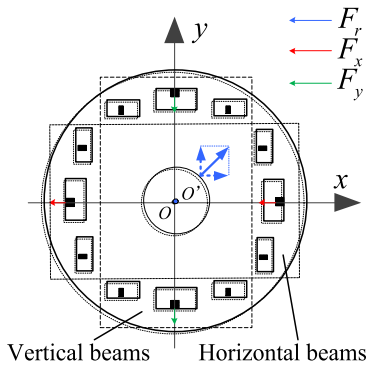

(a) Small rotor vibration

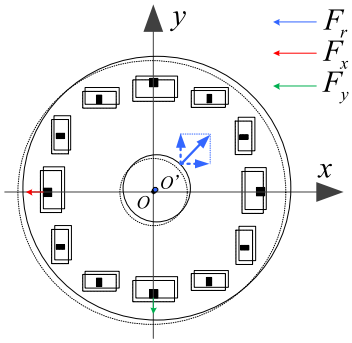

(b) Middle rotor vibration

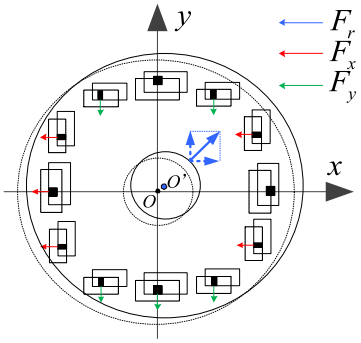

(c) Large rotor vibration

Fig. 2. Piecewise linear positive stiffness schematic diagram under different rotor vibrations.

Table 1
Positive stiffness parameters.

Parameter	Value	Parameter	Value
k_a	5000 N/m	e_a	0.2 mm
k_b	6250 N/m	e_b	0.9 mm
k_c	40 N/m		

According to the positive stiffness of each segment, the resultant force applied to the MNES can be expressed as

$$F_z(e)=\begin{cases}2k_a|e|\,\mathrm{sgn}(e) & (|e|\le e_a)\\ 2k_a|e_a|\,\mathrm{sgn}(e)+k_a(|e|-e_a)\mathrm{sgn}(e) & (e_a\le|e|\le e_b)\\ 2k_a|e_a|\,\mathrm{sgn}(e)+k_a(|e|-e_a)\mathrm{sgn}(e)+4k_b(|e|-e_b)\mathrm{sgn}(e) & (|e|>e_b)\end{cases} \tag{3}$$

Using the parameter of the positive stiffness in Table 1, the relationship between the MNES displacement and the piecewise linear force can be obtained and shown in Fig. 3.

The negative force F_f provided by the magnetic spring can be calculated by using equivalent magnetic charge method [28]. The negative force F_f is provided by the magnetic spring. The magnetic spring is made up of ring type magnets, which are divided into outer magnets and central magnets, as shown in Fig. 4(a). The outer diameter, inner diameter and thickness of the outer magnets are R_{D1}, R_{d1} and b_1, and those of the central magnets are R_{D2}, R_{d2} and b_2, respectively. The distance between the outer magnet and the central magnet is h. The width of the connecting part is B.

The magnetic spring axial diagram of the plane 2 and plane 3 is shown in Fig. 4(b). The radius of the point charges on plane 2 and plane 3 are r_2 and r_3, respectively. The relation vector of the plane 2 point charge and plane 3 point charge is $\boldsymbol{r}_{23}$. The angles of the point charges on plane 2 and plane 3 are α and β, respectively. The radial distance between central magnets and outer magnets is e. The magnetic force of magnetic plane 3 on magnetic plane 2 is F_{23}. The magnetic force of magnetic plane 2 on magnetic plane 3 is F_{32}.

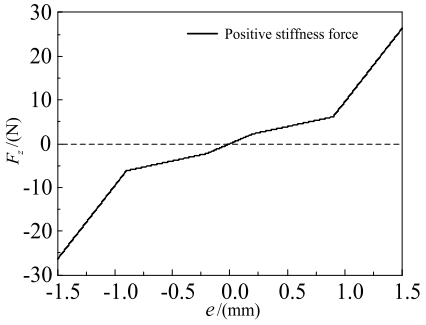

Fig. 3. Relationship between the MNES displacement and piecewise linear force.

When the central magnets are in non-centre position, they will be subjected to a radial repulsive force. As shown in Fig. 4(b), according to the equivalent magnetic charge method, the point charge q_2 of a point (r_2,α) in plane 2 is

$$q_2 = B_r r_2 \mathrm{d}r_2 \mathrm{d}\alpha \tag{4}$$

where, B_r represents the residual flux density.

The point charge q_3 of a point (r_3,β) in plane 3 is

$$q_3 = B_r r_3 \mathrm{d}r_3 \mathrm{d}\beta \tag{5}$$

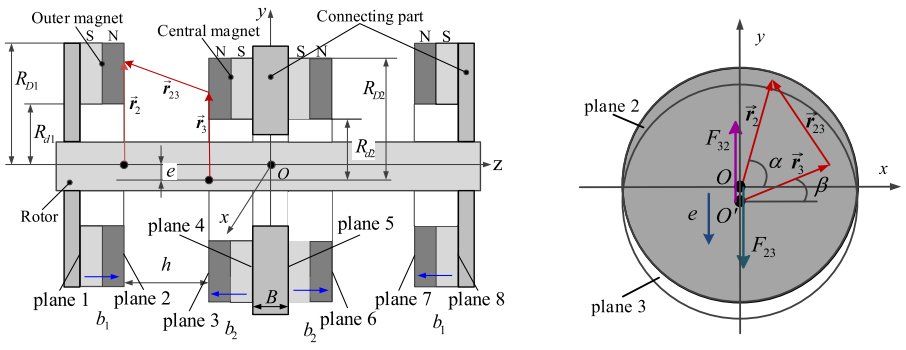

(a) Structure diagram of the magnetic spring (b) Axial diagram of the magnetic plane 2 and plane 3.

Fig. 4. Schematic diagram of the negative stiffness.

The electrostatic force of interaction $\mathrm{d}\overrightarrow{F_{23}}$ between the two points is

$$\mathrm{d}\overrightarrow{F_{23}} = \frac{B_r^2}{4\pi\mu_0}\frac{r_2 r_3 \mathrm{d}r_2 \mathrm{d}\alpha \mathrm{d}r_3 \mathrm{d}\beta}{r_{23}^2}\overrightarrow{r_{23}} \tag{6}$$

where, μ_0 represents the relative permeability of the permanent magnets.

According to the derivation result in [28], when the central magnets move a distance e along the radial direction of the magnets, the interaction force of magnetic plane 3 on magnetic plane 2 is F_{23} in the same direction of e. The interaction force F_{23} is

$$F_{23} = \frac{B_r^2}{4\pi\mu_0}\int_0^{2\pi}\int_0^{2\pi}\int_{R_{d1}}^{R_{D1}}\int_{R_{d2}}^{R_{D2}}\frac{A_{23}}{\left(B_{23}+C_{23}+D_{23}\right)^{3/2}}\mathrm{d}r_2\mathrm{d}r_3\mathrm{d}\alpha\mathrm{d}\beta \tag{7}$$

where, $A_{23} = r_2 r_3(r_3\cos\beta - r_2\cos\alpha - e)$, $B_{23} = (r_3\cos\beta - r_2\cos\alpha - e)^2$, $C_{23} = (r_3\sin\beta - r_2\sin\alpha)^2$ and $D_{23} = h^2$.

Similarly, the interaction forces of magnetic plane i $(i = 4-8)$ on magnetic plane 2 is F_{2i} in the same direction of e. The interaction force F_{2i} is

$$F_{2i} = (-1)^{i+1}\frac{B_r^2}{4\pi\mu_0}\int_0^{2\pi}\int_0^{2\pi}\int_{R_{d1}}^{R_{D1}}\int_{R_{d2}}^{R_{D2}}\frac{A_{2i}}{\left(B_{2i}+C_{2i}+D_{2i}\right)^{3/2}} \times \mathrm{d}r_2\mathrm{d}r_i\mathrm{d}\alpha\mathrm{d}\beta \quad (i = 4,\ldots,8) \tag{8}$$

where, $h_{23} = h$, $h_{24} = h + b_2$, $h_{25} = h + b_2 + B$, $h_{26} = 2h + b_2 + B$, $A_{2i} = r_2 r_i(r_i\cos\beta - r_2\cos\alpha - e)$, $B_{2i} = (r_i\cos\beta - r_2\cos\alpha - e)^2$, $C_{2i} = (r_i\sin\beta - r_2\sin\alpha)^2$ and $D_{2i} = h_{2i}^2$.

Also, the interaction forces of magnetic plane i $(i = 3-8)$ on magnetic plane 1 is F_{1i} in the same direction of e. The interaction force F_{1i} can be calculated similar as Eq. (7).

$$F_{1i} = (-1)^{i}\frac{B_r^2}{4\pi\mu_0}\int_0^{2\pi}\int_0^{2\pi}\int_{R_{d1}}^{R_{D1}}\int_{R_{d2}}^{R_{D2}}\frac{A_{1i}}{\left(B_{1i}+C_{1i}+D_{1i}\right)^{3/2}} \times \mathrm{d}r_1\mathrm{d}r_i\mathrm{d}\alpha\mathrm{d}\beta \quad (i = 3,\ldots,8) \tag{9}$$

where, $A_{1i} = r_1 r_i(r_i\cos\beta - r_1\cos\alpha - e)$, $B_{1i} = (r_i\cos\beta - r_1\cos\alpha - e)^2$, $C_{1i} = (r_i\sin\beta - r_1\sin\alpha)^2$ and $D_{1i} = \left(b + h_{2i}\right)^2$.

Moreover, the magnetic spring structure described above is a bilaterally symmetrical structure, so the repulsive forces on the left and right sides of the central magnets are equal. The total reaction force of the outer magnets to the central magnets is

$$F_f(e) = 2\sum_{i=3}^{8}\left(F_{1i} + F_{2i}\right) \tag{10}$$

Using the parameter in Table 2, the negative force F_f applied to the MNES can be expressed as

$$F_f(e) = -7022e - 4.1\times10^{-10}e^2 + 8.16\times10^{6}e^3 \tag{11}$$

Table 2
Negative stiffness parameters.

Parameter	Value	Parameter	Value
B_r	1.34 T	B	5 mm
R_{D1}	25 mm	b_1	12 mm
R_{d1}	12.5 mm	b_2	6 mm
R_{D2}	25 mm	μ_0	$4\pi\times10^{-7}$ N/A^2
R_{d2}	12.5 mm	h	12.8 mm

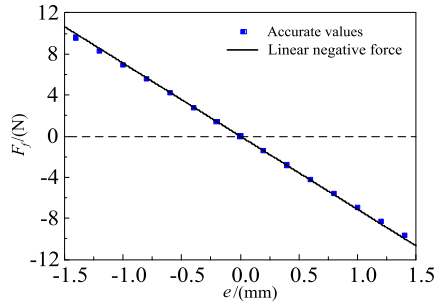

Fig. 5. Comparison of the linear negative force and the accurate values.

When e is very small, the linear part of the negative force is much larger than the nonlinear parts, so only the linear part is considered and the negative force can be expressed as

$$F_f(e) = -7022e \tag{12}$$

So, the negative stiffness can be expressed as

$$k_f = \frac{\mathrm{d}F_f(e)}{\mathrm{d}e} = -7022 \tag{13}$$

The negative force accurate values are calculated by Eq. (11), and the simplified linear negative force is calculated by Eq. (12). Comparing the linear force generated by negative stiffness with the accurate values, the resulting relationship is shown in Fig. 5.

The multi-stable piecewise linear force F_d can be calculated by Eqs. (1), (3) and (12). As shown in Fig. 6, the MNES have five points (A, B, C, D, E) with zero force, which means MNES are five equilibrium positions. Among them, A, C and E are stable equilibrium positions, B and D are unstable equilibrium positions.

2.3. The rotor-MNES system dynamic model

Using the lumped mass method, the dynamic model of rotor system with the MNES is shown in Fig. 7, and the axial diagram of rotor-MNES

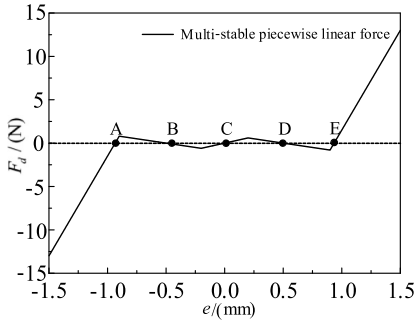

Fig. 6. Relationship between the MNES displacement and multi-stable piecewise linear force.

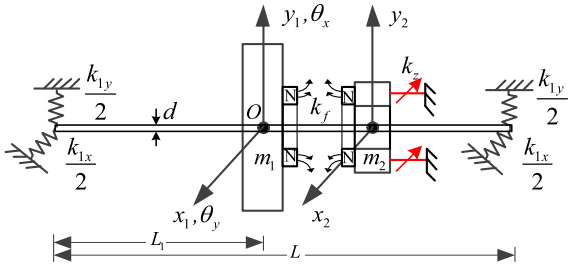

Fig. 7. Simplified model of the rotor-MNES system.

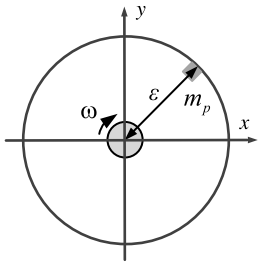

Fig. 8. Axial diagram of the rotor-MNES system model.

system model is shown in Fig. 8. According to the result in Appendix, the dynamic differential equations are written as

$$\begin{cases} m_1\ddot{x}_1 + (c_{1x}+c_{2x})\dot{x}_1 - c_{2x}\dot{x}_2 + k_{rf}\theta_y + (k_{1x}+k_f)x_1 - k_f x_2 \\ \quad = m_p\varepsilon\omega^2\cos(\omega t) \\ m_1\ddot{y}_1 + (c_{1y}+c_{2y})\dot{y}_1 - c_{2y}\dot{y}_2 - k_{rf}\theta_x + (k_{1y}+k_f)y_1 - k_f y_2 \\ \quad = m_p\varepsilon\omega^2\sin(\omega t) \\ J_d\ddot{\theta}_x + \omega J_p\dot{\theta}_y - k_{fr}y + k_{ff}\theta_x = 0 \\ J_d\ddot{\theta}_y - \omega J_p\dot{\theta}_x + k_{fr}x + k_{ff}\theta_y = 0 \\ m_2\ddot{x}_2 - c_{2x}(\dot{x}_1 - \dot{x}_2) - k_f x_1 + F_d(x_2) = 0 \\ m_2\ddot{y}_2 - c_{2x}(\dot{y}_1 - \dot{y}_2) - k_f y_1 + F_d(y_2) = 0 \end{cases} \tag{14}$$

where, "·" denotes d/dt. x_1 and y_1 are displacements of the disc in the horizontal and vertical directions, respectively. x_2 and y_2 are displacements the MNES mass in the horizontal and vertical directions, respectively. θ_x, θ_y are the angle of the disc in the horizontal and vertical directions, respectively. m_1 and m_2 are the masses of the rotor system and the MNES, respectively. J_d, J_p are radial moment of inertia, polar moment of inertia of the disc, respectively. c_{1x} and c_{1y} are the damping of the rotor system in the horizontal and vertical directions, respectively. c_{2x} and c_{2y} are the damping of the ring magnets in the horizontal and vertical directions, respectively. k_{1x}, k_{1y}, k_{rf}, k_{fr}, k_{ff} are stiffness of bending and torsional of the rotor, respectively. m_p, ω and ε are the eccentric quality, the rotor speed and the eccentricity, respectively.

Table 3
Dimensional parameters of the Bently Nevada RK4 test rig.

Parameter	Value	Parameter	Value
d	0.01 m	L	0.38 m
D_{disc}	0.08 m	H_{disc}	0.02 m
L_1	0.19 m	ρ	7.9×10^3 kg/m^3
ε	0.04 m		

Table 4
Dynamic parameters of the Bently Nevada RK4 test rig.

Parameter	Value	Parameter	Value
m_1	1 kg	J_p	8×10^{-4} kg m^2
J_d	4×10^{-4} kg m^2	k_{1x}	8.9×10^4 N/m
k_{1y}	8.9×10^4 N/m	k_{rf}	0 N/m
k_{fr}	0 N/m	k_{ff}	3250 N/m
c_{1x}	3 N s/m	c_{1y}	3 N s/m

3. Numerical simulation and analysis

3.1. Parameter definition

(1) Parameters of the rotor system

The rotor system dimensional parameters are taken from the Bently RK4 test rig. In Table 3, d and L are the length and diameter of the rotor shaft, respectively. ρ, D_{disc} and H_{disc} are the density, diameter and thickness of the disc, respectively. L_1 is the distance from the disc to the bearing.

In Table 4, the bending stiffness and torsional stiffness of the rotor are calculated by the equations in Appendix. The damping coefficients are identified by the modal test of the rotor system.

(2) Parameters of the MNES

The MNES mass is selected as $m_2 = 0.1$ kg. The damping of the ring magnets is $c_{2x} = c_{2y} = 2$ N s/m. The other parameters are shown in Tables 1 and 2.

3.2. Transient vibration suppression analysis of the rotor-MNES system

In this section, the numerical simulations of the rotor-MNES system adopt parameters in Section 3.1 and the initial conditions are zero for each variable except for variables x_1 or y_1 (see below). In the transient analysis, m_p should be equal to zero to prevent the harmonic, and different transient energies will be applied to the rotor-MNES system. At the same time, the responses of the rotor system with and without the MNES will be compared to confirm the vibration absorption capacity of the MNES.

(1) A 98 N pulse force

Assuming the rotor is given a 98 N pulse force in the horizontal or vertical direction, the rotor system will produce a 1.2 mm initial amplitude, that is, $x_1 = 1.2$ mm or $y_1 = 1.2$ mm at 0 s. The transient responses of the rotor system with and without the MNES are obtained by using the numerical calculation method.

As shown in Fig. 9, the vibration amplitude of the rotor system without NES performs a free-attenuation motion, and the initial input energy is dissipated by its own damping. The vibration amplitude attenuation speed is slow, and it takes about 0.92 s to decay to 0.3 mm.

When NES is added, it can be seen that the MNES has a strong inhibitory effect on the rotor system, as shown in Fig. 10(a) and (b). The vibration amplitude takes about 0.28 s to decay to 0.3 mm. The attenuation speed is 3.28 times as fast as that of the rotor system without the NES.

Initially, the rotor system and the MNES traverse multiple equilibrium positions (three sinks) and rapidly attenuate the energy to

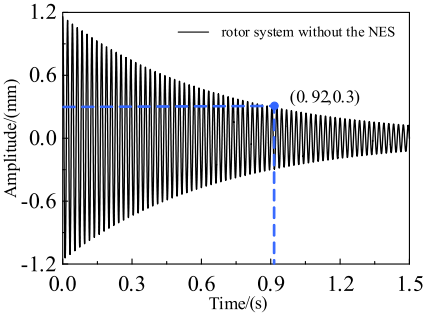

Fig. 9. Transient response of the rotor system under a 98 N pulse force.

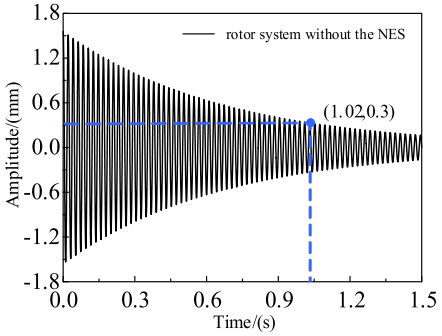

Fig. 11. Transient response of the rotor system under a 125 N pulse force.

complete the fully snap-through motion (0 s~0.15 s). During this period, only the snap-through motion [26,29,30] exists in the rotor system. Snap-through motion is a kind of energy transfer motion, which means the MNES quickly traverse the multiple equilibrium positions and jump among them. During snap-through motion, the MNES can bring about a large-amplitude vibration and shows a good performance in vibration absorption.

Then, energy of the rotor-MNES system is consumed between two adjacent stable equilibrium positions (0.15 s~0.67 s). This performance is a kind of sink-to-sink motion, and the MNES's motion contains two states. When the energy is large enough, the MNES will trigger the snap-through motion and consume energy; When the energy is small, the MNES vibrates at a single stable equilibrium point and consumes energy slowly.

Finally, the rotor-MNES system residual energy is dissipated at a single stable equilibrium point (0.67 s~1.0 s). This performance is a kind of in-sink motion, which cannot make the BNES trigger the snap-through motion. The MNES eventually stays at the stable equilibrium point C.

So, under the impact force, the energy consumption process of the MNES is divided into fully snap-through motion, sink-to-sink motion and in-sink motion, respectively.

(2) A 125 N pulse force

In order to verify that the MNES can absorb different impact energy, assuming the rotor is given a 125 N pulse force in the horizontal or vertical direction, the rotor system will produce a 1.5 mm initial amplitude, that is, $x_1 = 1.5$ mm or $y_1 = 1.5$ mm at 0 s. The transient responses of the rotor system with and without the MNES are as follows.

The vibration amplitude of the rotor system without the NES in Fig. 11 continues to be slow, and it takes about 1.02 s to decay to 0.3 mm.

As shown in Fig. 12(a) and (b), the MNES still has an obvious vibration absorption effect. After adding the MNES, the vibration amplitude of the rotor system experiences 0.28 s to decay to 0.3 mm. The speed is 3.64 times as fast as that of the rotor system without the NES. Comparing with the small impact energy, the attenuation speed is obviously improved. At the same time, under this force, the MNES (Fig. 12(b)) has a larger vibration amplitude and more time to traverse multiple equilibrium positions, indicating that more energy is transferred to the MNES and consumed in the vibration. The MNES eventually stays at the stable equilibrium position A. This phenomenon is due to the fact that there are multiple stable equilibrium positions in the rotor-MNES system, and the MNES will eventually stay at one of stable equilibrium positions based on the energy intake.

(3) A 142 N pulse force

In order to explore the effect of the MNES's final residence positions to absorb the impact energy, assuming the rotor is given a 142 N pulse force in the horizontal or vertical direction, it will produce a 1.8 mm initial amplitude, that is, $x_1 = 1.8$ mm or $y_1 = 1.8$ mm at 0 s. The transient responses of the rotor system with and without the MNES are as follows.

As shown in Fig. 13, the vibration amplitude of the rotor system without NES experiences 1.20 s to decay to 0.3 mm.

As shown in Fig. 14(a) and (b), the MNES has further enhanced the vibration absorption effect under this impact energy, and the rotor system with MNES experiences 0.32 s to reduce to 0.3 mm. The attenuation speed is 3.75 times as fast as that of the rotor system without the NES. The MNES eventually stays at the stable equilibrium position E. Comparing with Figs. 10(b), 12(b) and 14(b), the rotor system and the MNES eventually stay at three different sets of equilibrium positions. Under the same MNES and different impact energies, the MNES has a strong inhibitory effect on rotor system, regardless of which equilibrium position it eventually stops.

In summary, the MNES has a strong vibration suppression effect on the rotor system with different initial energies. After adding the MNES, the rotor system has a very fast amplitude attenuation, which is more than three times that of the rotor system without the MNES. Under

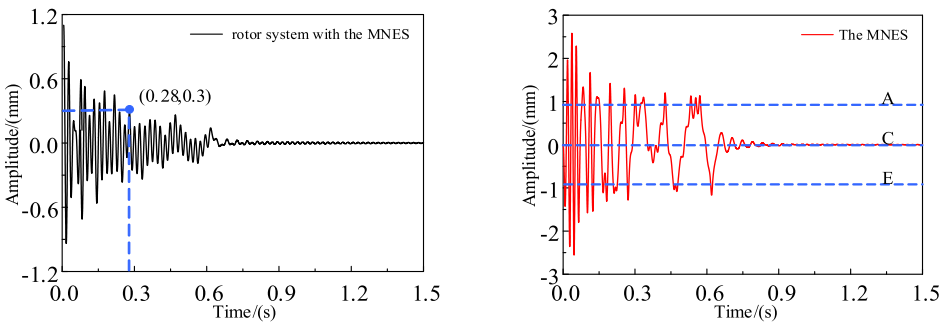

(a) Rotor system with the MNES (b) MNES

Fig. 10. Transient responses of the rotor-MNES system under a 98 N pulse force.

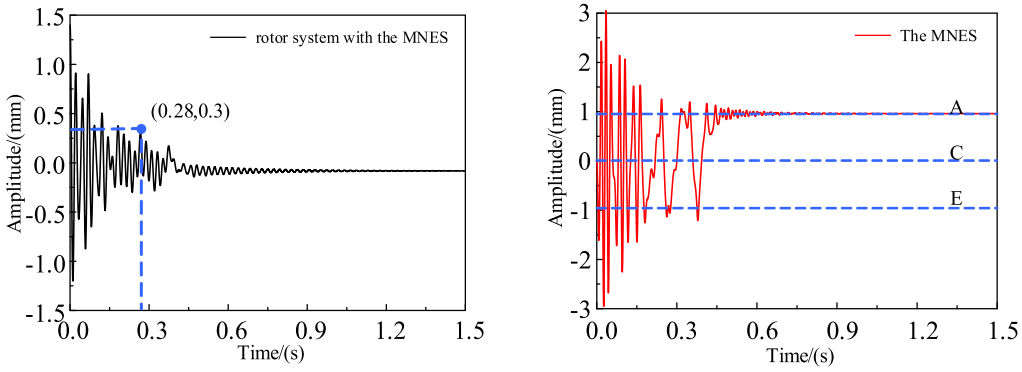

(a) Rotor system with the MNES (b) MNES

Fig. 12. Transient responses of the rotor-MNES system under a 125 N pulse force.

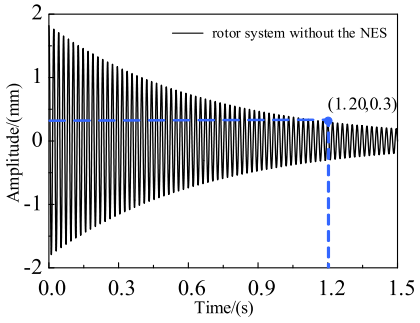

Fig. 13. Transient response of the rotor system under a 142 N pulse force.

the certain initial energy, the MNES absorbs the vibration generated by the rotor system, moves back and forth between different equilibrium positions, consumes energy through the MNES connection damping, and finally stays at a stable equilibrium position. Different initial energies will create different final stable equilibrium positions. But the final stable equilibrium positions do not affect the vibration suppression effect of the MNES on the rotor system.

3.3. Steady-state vibration suppression analysis of a rotor-MNES system

In this section, the numerical simulations of the rotor-MNES system adopt parameters in Section 3.1 and the initial conditions are zero for each variable except for variable m_p (see below). In the steady-state analysis, different m_p will be used to produce different periodic force. At the same time, the responses of the rotor system with and without MNES will be compared in frequency domain.

(1) $m_p = 3.5 \times 10^{-4}$ kg

Assuming the rotor system is isotropic. When the eccentric mass is $m_p = 3.5 \times 10^{-4}$ kg, the rotor system will generate a same periodic force in the vertical and horizontal directions. As far as the single direction is concerned, the rotor system without the MNES in Fig. 15(a) has a natural frequency around 47.5 Hz and a maximum amplitude of 1.33 mm.

As shown in Fig. 15(b), after adding the MNES, the overall suppression effect of the rotor system is obvious, and the maximum amplitude is 0.58 mm, so its vibration suppression rate is more than 56%. At the same time, the maximum amplitude of the MNES is 1.70 mm, which is much larger than that of the rotor system in the resonance region, indicating that the vibration energy of the rotor system is transferred to the MNES.

The rotor system and MNES in Fig. 15(b) have SMR [31] region in the frequency range of 46.3 Hz~49.0 Hz. Meanwhile, the time responses at 47.5 Hz are shown in Fig. 16(a) and (b). When the energy is small, the MNES will vibrate around a stable equilibrium position (such as 24.07~24.18 s). When the energy is large enough, the MNES will vibrate through multiple equilibrium positions (such as 24.67~24.77 s).

(2) $m_p = 4.0 \times 10^{-4}$ kg

In order to analyse the influence of the exciting force on the vibration suppression effect and SMR region, the eccentric mass is increased. When the eccentric mass is $m_p = 4.0 \times 10^{-4}$ kg, the rotor-MNES system is subjected to a stronger exciting force. The natural frequency of the

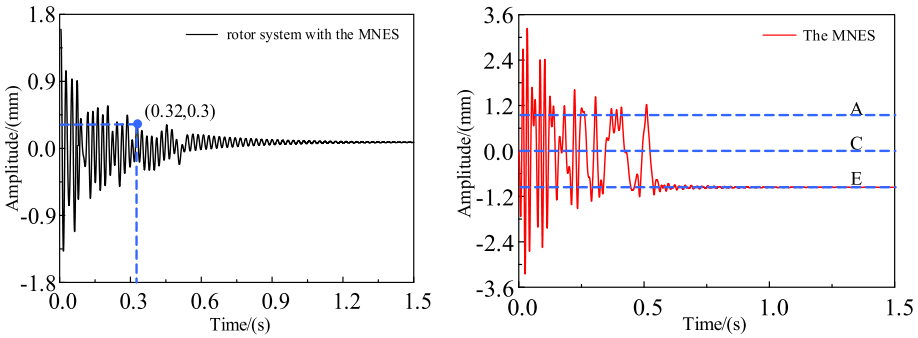

(a) Rotor system with the MNES (b) MNES

Fig. 14. Transient responses of the rotor-MNES system under a 142 N pulse force.

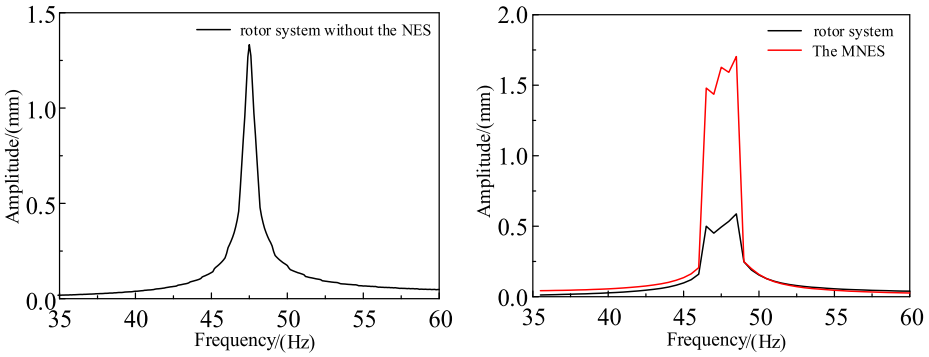

(a) Rotor system without the MNES (b) Rotor system with the MNES

Fig. 15. Frequency responses of the rotor and rotor-MNES systems under a small stable periodic exciting force.

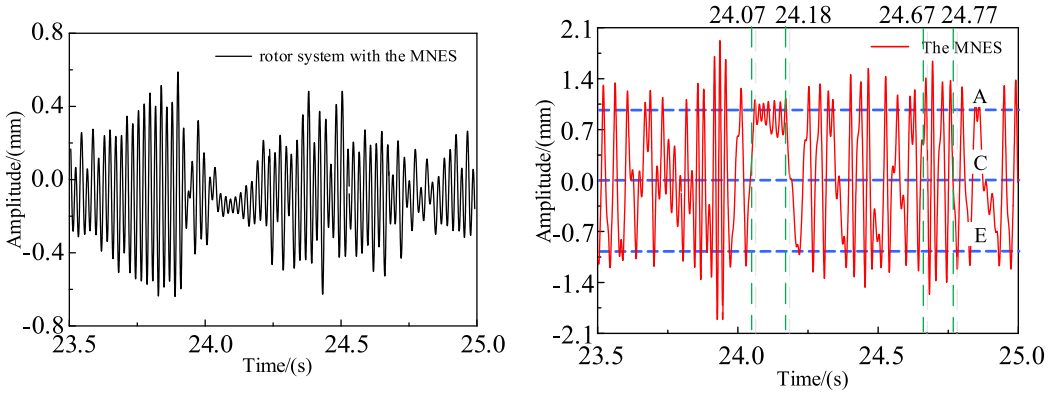

(a) Rotor system with the MNES (b) MNES

Fig. 16. Time responses of the rotor-MNES system under a small stable periodic variation force.

rotor system without MNES (Fig. 17(a)) is still around 47.5 Hz, and the maximum amplitude is 1.52 mm.

After adding the MNES, the maximum amplitude of the rotor system in Fig. 17(b) is 0.63 mm. Compared with the rotor system without the MNES, it is reduced by 58.6%, and it has stronger vibration suppression ability than small energy. At the same time, the MNES amplitude maximum is also increased to 1.89 mm, and the amplitude in resonance region is bigger than the MNES amplitude in Fig. 15(b). It can be seen that more energy is transferred to the MNES with the increase of excitation force.

As is shown in Fig. 17(b), there are SMR region between the rotor system and the MNES in the range of 46.2 Hz ~ 49.2 Hz, and a slightly wider suppression band than that of Fig. 15(b). Specifically, the time responses of 47.5 Hz are shown in Fig. 18(a) and (b).

(3) $m_p = 4.75 \times 10^{-4}$ kg

To further investigate the influence of the exciting force on the vibration suppression effect and SMR region, the eccentric mass is continuously increased. As shown in Fig. 19(a), when the eccentric mass is $m_p = 4.75\times10^{-4}$ kg, the maximum amplitude of the rotor system without the MNES is 1.81 mm.

After adding the MNES, the maximum amplitude of the rotor system in Fig. 19(b) is 0.70 mm, which is 61.3% lower than the rotor system without the MNES. It can be seen that the MNES still has a great vibration suppression effect on the large vibration energy, and the vibration suppression rate is still improved.

As shown in Fig. 19(b), the rotor system and the MNES have a SMR region in the frequency range of 45.4 Hz~50.0 Hz, and the time responses of 47.5 Hz are shown in Fig. 20(a) and (b).

In summary, the MNES has obvious suppression effect on the entire frequency domain range, especially in the resonance region, and the vibration suppression rate is above 56%. In a certain range of exciting force, as the excitation force increases, the vibration absorption effect of the MNES will increase, and the vibration suppression frequency band will also become wider.

3.4. Comparison between MNES and BNES

In this section, the numerical simulation parameters of x_2, y_2, k_f and F_d in Eq. (14) should be replaced by x_{bnes}, y_{bnes}, k_{fbnes} and F_{dbnes}, respectively. At the same time, the same transient energies as the rotor with the MNES will be applied to the rotor-BNES system, and the numerical simulation results of the rotor system with the MNES and the BNES will be compared to confirm the vibration absorption advantages of the MNES. The initial conditions are zero for each variable except for rotor initial amplitude (see below).

Comparing with the MNES, the magnetic BNES needs to use the nonlinear part stiffness of magnet, so the distance between the outer magnet and the central magnet must be very small. In such a case, the magnetic BNES can hardly stay at the centre and it needs an external force to balance at a stable equilibrium position.

In general, the magnetic BNES (Fig. 21) consists of a permanent magnet negative stiffness structure and a linear spring. When the BNES at stable equilibrium position C (Fig. 21(a)), the spring is in a stretch state. When the BNES is at stable equilibrium position E (Fig. 21(b)), the spring is in a compressed state.

In order to ensure the comparability of the MNES and BNES, the BNES is selected with same parameters as the MNES except the multi-stable force. So, the mass and damping of BNES are selected as m_{bnes} = 0.1 kg and c_{bnes} = 2 N s/m, respectively.

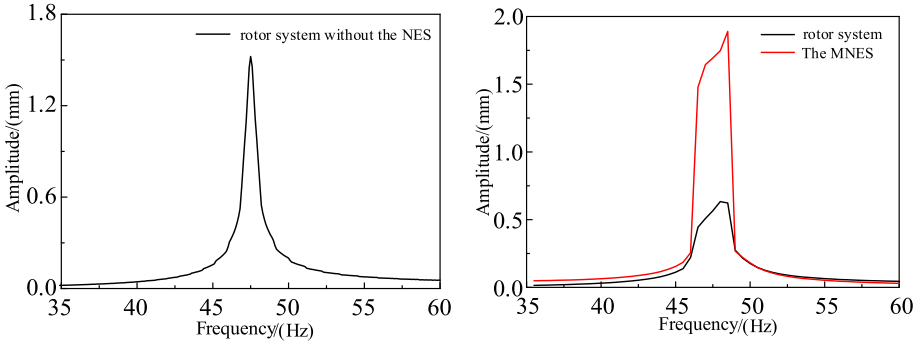

(a) Rotor system without the MNES (b) Rotor system with the MNES

Fig. 17. Frequency responses of the rotor and rotor-MNES systems under a middle stable periodic variation force.

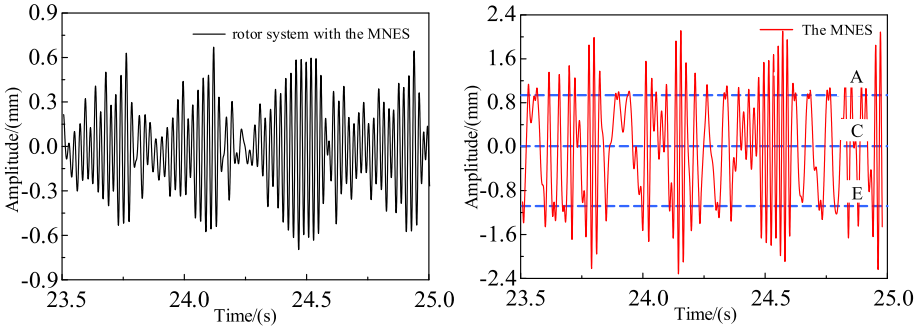

(a) Rotor system with the MNES (b) MNES

Fig. 18. Time responses of the rotor-MNES system under a middle stable periodic variation force.

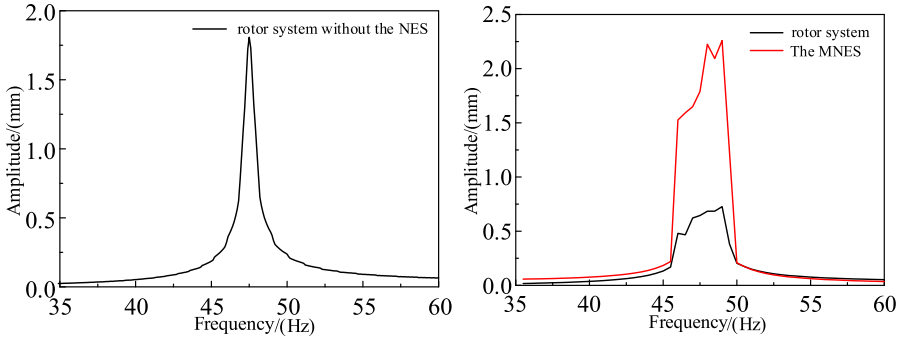

(a) Rotor system without the MNES (b) Rotor system with the MNES

Fig. 19. Frequency responses of the rotor and rotor-MNES systems under a large stable periodic variation force.

The BNES curve in Fig. 22 is fitted from MNES's multi-stable piecewise linear force data and reduces the number of equilibrium positions, ensuring the same stiffness between the equilibrium positions of the bi-stable and multi-stable. The specific form is expressed as Eq. (15).

$$F_{dbnes}(e) = 1.5 \times 10^{10} e^3 - 2.07 \times 10^7 e^2 + 6348e \tag{15}$$

The bi-stable force in Eq. (15) is composed of magnet force and linear spring force. The specific magnet stiffness and linear spring stiffness are shown as Eq. (16) and Eq. (17), respectively.

$$k_{fbnes}(e) = 4.5 \times 10^{10} e^2 - 4.14 \times 10^7 e \tag{16}$$

$$k_{zbnes}(e) = 6348 \tag{17}$$

The responses of the rotor system with the BNES can be calculated by using Eqs. (9), (15), (16) and (17). Assuming the rotor is given a 98N, 125N or 142 N pulse force in the horizontal or vertical direction, it will produce a 1.2 mm, 1.5 mm or 1.8 mm initial amplitude in x or y direction at 0 s. After adding BNES, the rotor system vibration amplitude in Fig. 23(a), (b) and (c) experience about 0.30 s, 0.43 s and 0.51 s to decrease to 0.3 mm, and the attenuation speed are 3.06 times, 2.37 times and 2.35 times as fast as that of the rotor system without the NES, respectively.

Comparing with BNES, the MNES has a more obvious suppression effect. The rotor system with the MNES in Figs. 10(b), 12(b) and 14(b) experience about 0.28 s, 0.28 s and 0.32 s to 0.3 mm, respectively. The attenuation speed are 1.07 times, 1.54 times and 1.63 times as fast as that of the rotor system with the BNES, respectively.

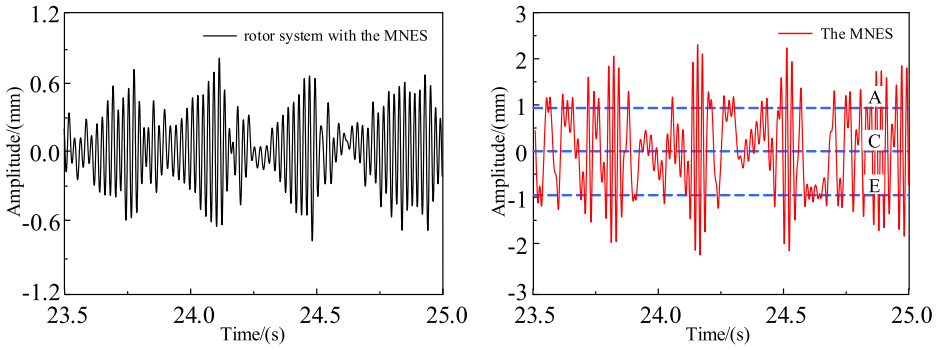

(a) Rotor system with the MNES (b) MNES

Fig. 20. Time responses of the rotor-MNES system under a large stable periodic variation force.

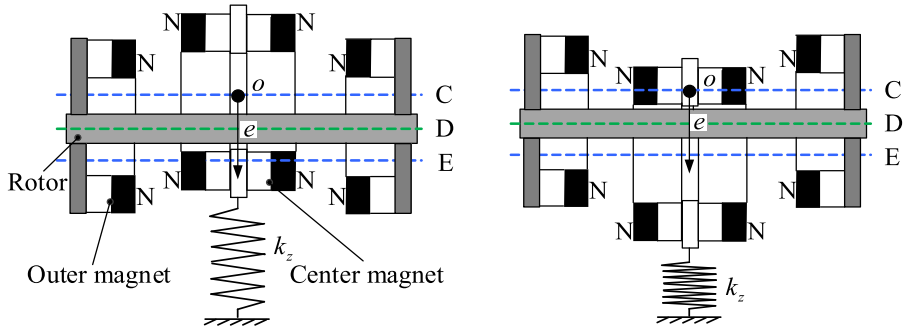

(a) State of the BNES at point C (b) State of the BNES at point E

Fig. 21. Schematic model of the rotor-BNES system.

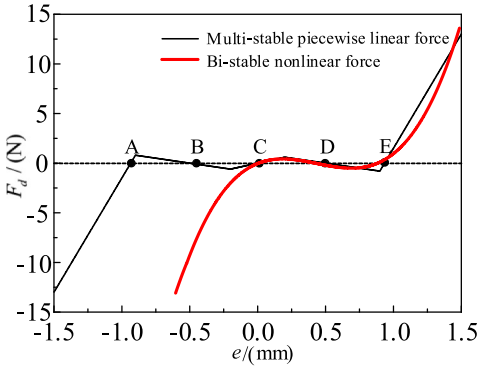

Fig. 22. Force of the bi-stable stiffness and multi-stable piecewise linear force.

As the impact energy increases, the MNES vibration suppression effect gradually increases, and the BNES vibration suppression effect gradually weakens. So, in a certain energy range, the MNES has better vibration suppression effect and can withstand a stronger impact energy than the BNES with the same stiffness between the equilibrium positions.

But the present structure is more complicated than BNES type, and also, the present structure is too large in the axial direction of the rotor system, which affects the actual application in rotor system, so these are the shortcomings of the present structure.

4. Experiments

4.1. Experiment setup

The vibration suppression effect experiment of the MNES is completed on the Bently rotor test rig. In this experiment, the MNES is mounted on the single-disc rotor system, as shown in Fig. 24(a). The experimental devices consist of a single disc rotor system, a MNES, two eddy current sensors, a photoelectric encoder, and a set of NI acquisition devices.

The MNES (Fig. 24(b)) is designed according to the parameters in Tables 1 and 2. In order to reduce the interference of the friction on the experiment, the lubricating oil is added to the place where MNES is in contact with the beams. At the same time, the photoelectric system, the eddy current sensor and the NI acquisition card are used to test the vibration frequency, test vibration displacement of the rotor system and complete the data acquisition, respectively.

4.2. Experimental results

4.2.1. Transient verification experiment

In this section, the initial experiment conditions are the same as Section 3.2. Different pulse forces are applied to the rotor system in the horizontal direction by the force hammer, and the obtained transient attenuation curves are compared with the simulation results.

The eddy current sensors can only measure the relative displacement, so the final equilibrium amplitude of the experiment is zero. The Fig. 25 characterizes the relationship between experimental rotor vibration amplitude and time under different pulse forces. The measured experimental transient responses have the same trends as simulated transient responses. They all traverse multiple steady-state points for

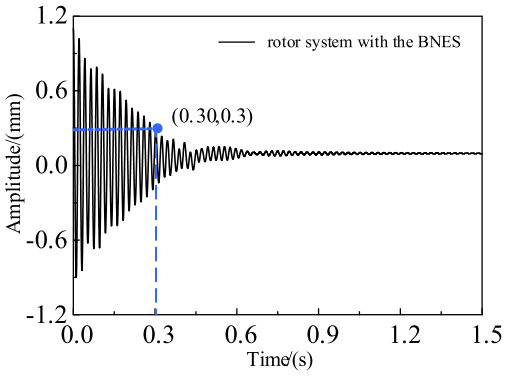

(a) A 98 N pulse force

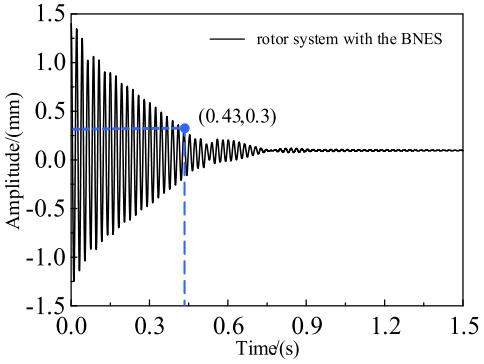

(b) A 125 N pulse force

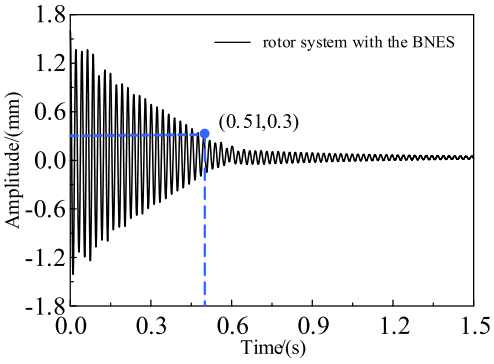

(c) A 142 N pulse force

Fig. 23. Transient responses of the rotor system with the BNES under different pulse forces.

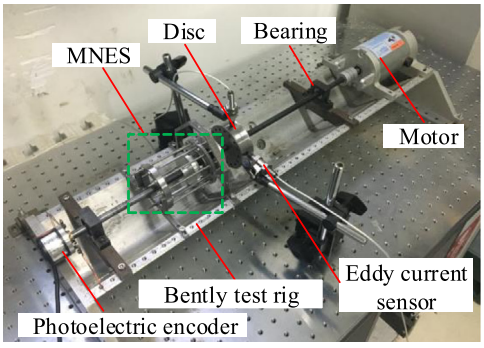

(a) Rotor system with the MNES

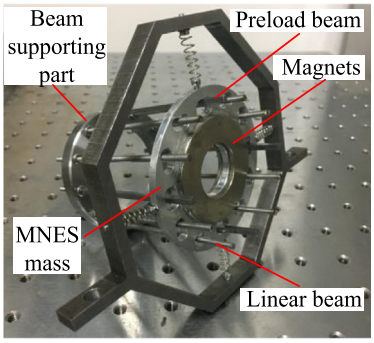

(b) MNES

Fig. 24. Experimental devices.

rapid energy decay, then consume energy between adjacent two stable equilibrium points, and finally deplete the remaining energy at a stable equilibrium position.

The experimental and simulated attenuation rates are compared as follows: as shown in Fig. 25(a), (b) and (c), under the experimental conditions of three different energies, the rotor system amplitudes experienced 0.77 s, 0.73 s and 0.83 s decays to zero, respectively. As shown in Figs. 10(a), 12(a) and 14(a), under the simulated conditions of three different energies, the rotor system amplitudes experienced 0.71 s, 0.71 s and 0.91 s to decay to zero, respectively.

Therefore, the attenuation rates of the rotor system are almost the same under experimental and simulated conditions.

4.2.2. *Steady-state verification experiment*

In this section, the initial experiment conditions are the same as Section 3.3. The eccentric disc with eccentric mass $m_p = 4.75 \times 10^{-4}$ kg is used to generate a stable periodic force, and the vibration suppression effects of the MNES in the vertical and horizontal directions of the rotor system are explored.

The Bently rotor system is isotropic, so the rotor system without the MNES has the same responses in the horizontal and vertical directions.

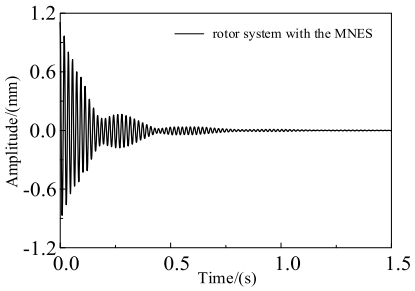

(a) A 98 N pulse force

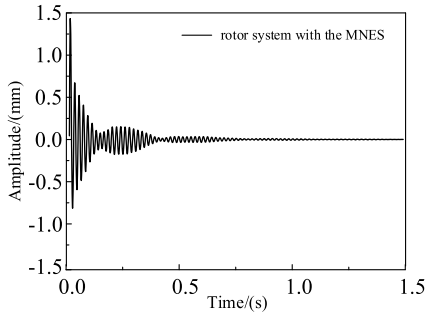

(b) A 125 N pulse force

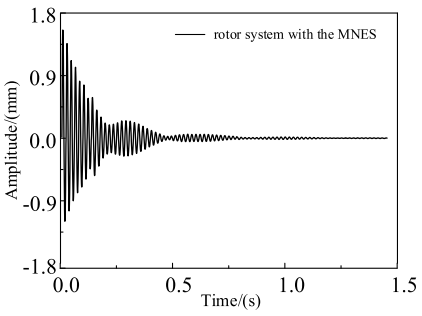

(c) A 142 N pulse force

Fig. 25. Transient experimental responses of the rotor system with the MNES under different pulse forces.

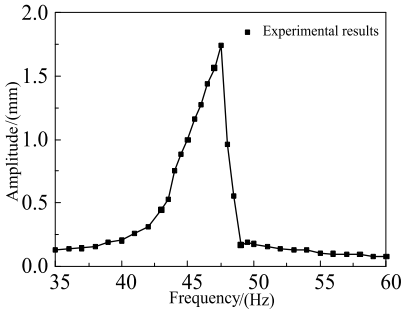

Fig. 26. Experimental frequency response of the rotor system without the MNES under a large stable periodic variation force in the horizontal and vertical directions.

As shown in Fig. 26, the rotor system without the MNES generates a maximum amplitude of 1.73 mm at the resonance region of 47.5 Hz.

Adding the MNES, the horizontal and vertical experimental results of the rotor system in Fig. 27(a) and (b) have the same trends as the simulation curves. The maximum vibration amplitudes of the two directions are 0.783 mm and 0.802 mm, respectively, so the vibration suppression rates reach 54.7% and 53.6%, respectively.

The rotor system with the MNES causes SMR regions in the range of 45.7 Hz~51 Hz and 45 Hz~50 Hz, respectively. Their specific time domain responses of 47.5 Hz are shown in Fig. 28(a) and (b).

So, the steady-state experiments demonstrate that the MNES has a strong vibration suppression effect and realizes the rotor system vibration suppression in a wide frequency domain.

5. Conclusion

In this paper, a grounded multi-stable nonlinear energy sink applied to the rotor system is proposed. The principles and fundamental characteristics of the MNES are studied numerically and experimentally. The mainly results are as follows:

(1) The designed MNES has a strong vibration suppression effect on the small amplitude's rotor system and can withstand a wide range of energy.

(2) In a certain range of exciting force, as the excitation force increases, the vibration absorption effect of the MNES will increase, and the vibration suppression frequency band will also become wider.

(3) In a certain energy range, the MNES has better vibration suppression effect and can withstand a stronger impact energy than the BNES with the same stiffness between the equilibrium positions.

(4) The final stable equilibrium position of the MNES does not affect the vibration suppression effect of the MNES on the rotor system.

Declaration of competing interest

The authors declare that they have no known competing financial interests or personal relationships that could have appeared to influence the work reported in this paper.

Acknowledgements

The authors would like to gratefully acknowledge the National Natural Science Foundation of China (Grant No. U1708257) and the Fundamental Research Funds for Central Universities (Grant No. N180313009) for the financial support for this study.

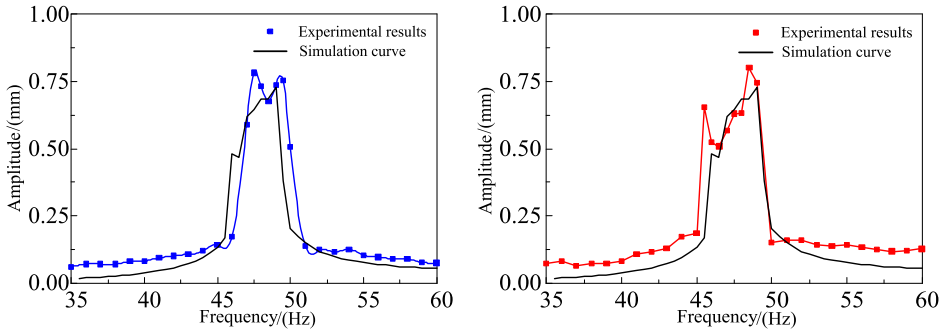

(a) Frequency response of the rotor system with the MNES in the horizontal direction

(a) Frequency response of the rotor system with the MNES in the vertical direction

Fig. 27. Experiment and simulation frequency responses of the rotor system with the MNES under a large stable periodic variation force in the horizontal and vertical directions.

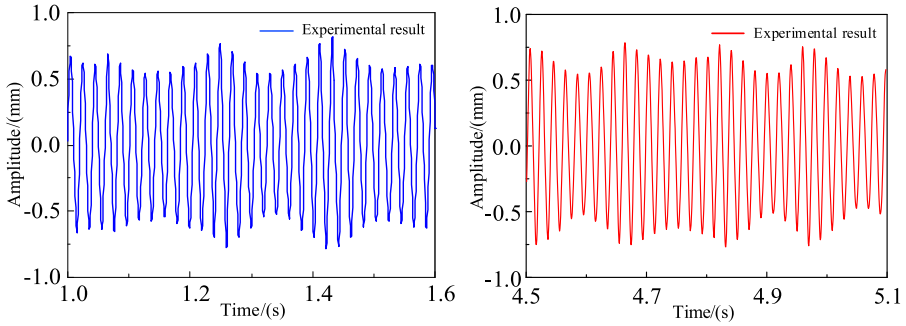

(a) Time response of the rotor system with the MNES in the horizontal direction

(b) Time response of the rotor system with the MNES in the vertical direction

Fig. 28. Experimental time responses of the rotor system with the MNES under a large stable periodic variation force in the horizontal and vertical directions.

Appendix

Axial vibration has little effect on the rotor, so the rotor system only needs to consider the following four degrees of freedom.

$$[x_1, y_1, \theta_x, \theta_y] \tag{A.1}$$

MNES does not rotate and has no axial vibration in the working process, so the degrees of freedom are as follows:

$$[x_2, y_2] \tag{A.2}$$

The Lagrange equation of the rotor-MNES system is

$$\frac{d}{dt}\left(\frac{\partial T}{\partial \dot{q}_i}\right) - \frac{\partial T}{\partial q_i} = Q_i \quad i = 1, 2, \ldots \mathrm{n} \tag{A.3}$$

where, the generalized coordinates are $q_1 = x_1$, $q_2 = x_2$, $q_3 = y_1$, $q_4 = y_2$, $q_5 = \theta_x$ and $q_6 = \theta_y$.

Total kinetic energy of rotor-MNES system is

$$T = T_1 + T_2 \tag{A.4}$$

Kinetic energy of rotor system is

$$T_1 = \frac{1}{2}m_1\left(\dot{x}_1^2 + \dot{y}_1^2\right) + \frac{1}{2}\left[J_d\left(\dot{\theta}_x^2 + \dot{\theta}_y^2\right) + J_p\omega^2 - 2J_p\omega\dot{\theta}_y\theta_x\right] \tag{A.5}$$

where, $J_p = \frac{1}{2}m_1R^2$, and $J_d = \frac{1}{2}J_p$.

Kinetic energy of MNES system is

$$T_2 = \frac{1}{2}m_2\left(\dot{x}_2^2 + \dot{y}_2^2\right) \tag{A.6}$$

According to the definition of generalized force, generalized force can be obtained.

$$Q_1 = m_p\varepsilon\omega^2\cos(\omega t) - (c_{1x}+c_{2x})\dot{x}_1 + c_{2x}\dot{x}_2 - k_{rf}\theta_y - (k_{1x}+k_f)x_1 + k_f x_2 \tag{A.7}$$

$$Q_2 = m_p\varepsilon\omega^2\sin(\omega t) - (c_{1y}+c_{2y})\dot{y}_1 + c_{2y}\dot{y}_2 + k_{rf}\theta_x - (k_{1y}+k_f)y_1 + k_f y_2 \tag{A.8}$$

$$Q_3 = c_{2x}(\dot{x}_1 - \dot{x}_2) + k_f x_1 - (k_f + k_z)x_2 \tag{A.9}$$

$$Q_4 = c_{2x}(\dot{y}_1 - \dot{y}_2) + k_f y_1 - (k_f + k_z)y_2 \tag{A.10}$$

$$Q_5 = k_{fr}y - k_{ff}\theta_x \tag{A.11}$$

$$Q_6 = -k_{fr}x - k_{ff}\theta_y \tag{A.12}$$

where, stiffness coefficient k_{rr}, k_{rf}, k_{fr} and k_{ff} are obtained by flexibility method.

According to the bending deformation formula of the beam, when the force P acts on the point O of the rotor, the deflection and the section corner of point O are respectively:

$$w_1 = -\frac{P(L-L_1)L_1}{6LEI}\left[L^2 - (L-L_1)^2 - L_1^2\right] \tag{A.13}$$

$$\varphi_1 = -\frac{P(L-L_1)}{2LEI}\left[\frac{1}{3}L^2 - \frac{1}{3}(L-L_1)^2 - L_1^2\right] \tag{A.14}$$

where, $I = \frac{1}{64}\pi d^4$, and $E = 206$ GPa.

When the moment M acts on the point O of the rotor, the deflection and the section corner of point O are respectively:

$$w_2 = \frac{ML_1}{6LEI}\left[L^2 - L_1^2 - 3(L-L_1)^2\right] \tag{A.15}$$

$$\varphi_2 = \frac{M}{6LEI}\left[L^2 - 3(L-L_1)^2 - 3L_1^2\right] \tag{A.16}$$

Therefore, the deflection or section corner at point O caused by unit force or moment, that is, the flexibility coefficients are:

$$\alpha_{rr} = -\frac{(L-L_1)L_1}{6LEI}\left[L^2 - (L-L_1)^2 - L_1^2\right] \tag{A.17}$$

$$\alpha_{r\varphi} = -\frac{(L-L_1)}{2LEI}\left[\frac{1}{3}L^2 - \frac{1}{3}(L-L_1)^2 - L_1^2\right] \tag{A.18}$$

$$\alpha_{\varphi r} = \frac{L_1}{6LEI}\left[L^2 - L_1^2 - 3(L-L_1)^2\right] \tag{A.19}$$

$$\alpha_{\varphi\varphi} = \frac{1}{6LEI}\left[L^2 - 3(L-L_1)^2 - 3L_1^2\right] \tag{A.20}$$

The stiffness matrix is the inverse of the flexibility matrix. The stiffness matrix is:

$$\begin{bmatrix} k_{rr} & k_{rf} \\ k_{fr} & k_{ff} \end{bmatrix} = \begin{bmatrix} \alpha_{rr} & \alpha_{r\varphi} \\ \alpha_{\varphi r} & \alpha_{\varphi\varphi} \end{bmatrix}^{-1} \tag{A.21}$$

By substituting kinetic energy and generalized force into (A.3), the dynamic model of rotor-MNES can be obtained.

$$\begin{cases} m_1\ddot{x}_1 + (c_{1x}+c_{2x})\dot{x}_1 - c_{2x}\dot{x}_2 + k_{rf}\theta_y + (k_{1x}+k_f)x_1 - k_f x_2 \\ \quad = m_p\varepsilon\omega^2\cos(\omega t) \\ m_1\ddot{y}_1 + (c_{1y}+c_{2y})\dot{y}_1 - c_{2y}\dot{y}_2 - k_{rf}\theta_x + (k_{1y}+k_f)y_1 - k_f y_2 \\ \quad = m_p\varepsilon\omega^2\sin(\omega t) \\ J_d\ddot{\theta}_x + \omega J_p\dot{\theta}_y - k_{fr}y_1 + k_{ff}\theta_x = 0 \\ J_d\ddot{\theta}_y - \omega J_p\dot{\theta}_x + k_{fr}x_1 + k_{ff}\theta_y = 0 \\ m_2\ddot{x}_2 - c_{2x}(\dot{x}_1 - \dot{x}_2) - k_f x_1 + F_d(x_2) = 0 \\ m_2\ddot{y}_2 - c_{2x}(\dot{y}_1 - \dot{y}_2) - k_f y_1 + F_d(y_2) = 0 \end{cases} \tag{A.22}$$

where, $k_{1x} = k_{1y} = k_{rr}$, $F_d(x_2) = (k_f + k_z)x_2$, and $F_d(y_2) = (k_f + k_z)y_2$.

References

[1] F.J.Doubrawa. Filho, M.A. Luersen, C.A. Bavastri, Optimal design of viscoelastic vibration absorbers for rotating systems, J. Vib. Control 17 (5) (2011) 699–710.

[2] H. Hu, L. He, Online control of critical speed vibrations of a single-span rotor by a rotor dynamic vibration absorber at different installation positions, J. Mech. Sci. Technol. 31 (5) (2017) 2075–2081.

[3] O.V. Gendelman, Y. Starosvetsky, M. Feldman, Attractors of harmonically forced linear oscillator with attached nonlinear energy sink i: description of response regimes, Nonlinear Dynam. 51 (1–2) (2008) 31–46.

[4] Y. Starosvetsky, O.V. Gendelman, Attractors of harmonically forced linear oscillator with attached nonlinear energy sink, II: Optimization of a nonlinear vibration absorber, Nonlinear Dynam. 51 (2008) 47.

[5] M. Weiss, A.T. Savadkoohi, O.V. Gendelman, et al., Dynamical behavior of a mechanical system including saint-venant component coupled to a non-linear energy sink, Int. J. Non-Linear Mech. 63 (2014) 10–18.

[6] O.V. Gendelman, Targeted energy transfer in systems with external and self-excitation, Proc. Inst. Mech. Eng., Part C 225 (9) (2011) 2007–2043.

[7] A.T. Savadkoohi, B. Vaurigaud, C.H. Lamarque, et al., Targeted energy transfer with parallel nonlinear energy sinks, part II: theory and experiments, Nonlinear Dyn. 67 (1) (2012) 37–46.

[8] B. Vaurigaud, A.T. Savadkoohi, C.H. Lamarque, Targeted energy transfer with parallel nonlinear energy sinks, part i: Design theory and numerical results, Nonlinear Dyn. 66 (4) (2011) 763–780.

[9] K. Yang, Y.W. Zhang, H. Ding, et al., Nonlinear energy sink for whole-spacecraft vibration reduction, J. Vib. Acoust. 139 (2) (2017) 021011.

[10] S. Bab, S.E. Khadem, M. Shahgholi, et al., Vibration attenuation of a continuous rotor-blisk-journal bearing system employing smooth nonlinear energy sinks, Mech. Syst. Signal Process. 84 (2017) 128–157.

[11] F. Nucera, M.D. McFarl, L.A. Bergman, et al., Application of broadband nonlinear targeted energy transfers for seismic mitigation of a shear frame: Computational results, J. Sound Vib. 329 (15) (2010) 2973–2994.

[12] E. Gourc, S. Seguy, G. Michon, et al., Chatter control in turning process with a nonlinear energy sink, Adv. Mater. Res. 698 (2013) 89–98.

[13] S. Bab, S.E. Khadem, M.K. Mahdiabadi, et al., Vibration mitigation of a rotating beam under external periodic force using a nonlinear energy sink (NES), J. Vib. Control 23 (6) (2017) 1001–1025.

[14] B. Bergeot, S. Bellizzi, B. Cochelin, Passive suppression of helicopter ground resonance using nonlinear energy sinks attached on the helicopter blades, J. Sound Vib. 392 (2017) 41–55.

[15] B. Bergeot, S. Bellizzi, B. Cochelin, Analysis of steady-state response regimes of a helicopter ground resonance model including a non-linear energy sink attachment, Int. J. Non-Linear Mech. 78 (2016) 72–89.

[16] H. Yao, D. Zheng, B. Wen, Magnetic nonlinear energy sink for vibration attenuation of unbalanced rotor system, Shock Vib. (2017).

[17] F. Romeo, G. Sigalov, L.A. Bergman, et al., Dynamics of a linear oscillator coupled to a bistable light attachment: numerical study, J. Comput. Nonlinear Dyn. 10 (1) (2014) 011007.

[18] P.O. Mattei, R. Ponçot, M. Pachebat, et al., Nonlinear targeted energy transfer of two coupled cantilever beams coupled to a bistable light attachment, J. Sound Vib. 373 (2016) 29–51.

[19] H. Yao, Z. Chen, B. Wen, Dynamic vibration absorber with negative stiffness for rotor system, Shock Vib. (2016).

[20] G. Habib, F. Romeo, The tuned bistable nonlinear energy sink, Nonlinear Dynam. 89 (1) (2017) 179–196.

[21] H. Wang, L. Tang, Modeling and experiment of bistable two-degree-of-freedom energy harvester with magnetic coupling, Mech. Syst. Signal Process. 86 (2017) 29–39.

[22] M. Panyam, M.F. Daqaq, Characterizing the effective bandwidth of tri-stable energy harvesters, J. Sound Vib. 386 (6) (2017) 336–358.

[23] S. Zhou, J. Cao, D.J. Inman, et al., Broadband tristable energy harvester: modeling and experiment verification, Appl. Energy 133 (2014) 33–39.

[24] S. Zhou, J. Cao, J. Lin, et al., Exploitation of a tristable nonlinear oscillator for improving broadband vibration energy harvesting, Eur. Phys. J.-Appl. Phys. 67 (3) (2014) 30902.

[25] L. Haitao, Q. Weiyang, L. Chunbo, et al., Dynamics and coherence resonance of tri-stable energy harvesting system, Smart Mater. Struct. 25 (1) (2016) 015001.

[26] Z. Zhou, W. Qin, P. Zhu, Improve efficiency of harvesting random energy by snap-through in a quad-stable harvester, Sensors Actuators A 243 (2016) 151–158.

[27] Z. Zhou, W. Qin, P. Zhu, A broadband quad-stable energy harvester and its advantages over bi-stable harvester: simulation and experiment verification, Mech. Syst. Signal Process. 84 (2017) 158–168.

[28] B. Han, S. Zheng, Y. Le, et al., Modeling and analysis of coupling performance between passive magnetic bearing and hybrid magnetic radial bearing for magnetically suspended flywheel, IEEE Trans. Magn. 49 (10) (2013) 5356–5370.

[29] A.F. Arrieta, P. Hagedorn, A. Erturk, et al., A piezoelectric bistable plate for nonlinear broadband energy harvesting, Appl. Phys. Lett. 97 (10) (2010) 104102.

[30] B. Ando, S. Baglio, C. Trigona, et al., Nonlinear mechanism in MEMS devices for energy harvesting applications, J. Micromech. Microeng. 20 (12) (2010) 125020.

[31] Y. Starosvetsky, O.V. Gendelman, Strongly modulated response in forced 2dof oscillatory system with essential mass and potential asymmetry, Physica D 237 (13) (2008) 1719–1733.